Applied Radiation and Isotopes 180 (2022) 110034

Contents lists available at ScienceDirect

Applied Radiation and Isotopes

journal homepage: www.elsevier.com/locate/apradiso

β-eye: A benchtop system for in vivo molecular screening of labeled compounds

E. Fysikopoulos [a,b,*], M. Rouchota [a,b], M. Georgiou [a], C. Sfyris [a], N. Cheimarios [a], S. Sarpaki [a], S. Kostopoulos [b], D. Glotsos [b], B. Larimer [c], C. Hunter [c], S. Lapi [c], H. Houson [c], A.V.F. Massicano [c], A. Sorace [c], E. Lamprou [a], G. Loudos [a]

[a] BIOEMTECH, Lefkippos Attica Technology Park - N.C.S.R Demokritos, Greece
[b] Biomedical Engineering Department, University of West Attica, Athens, Greece
[c] Small Animal Imaging Facility, Department of Radiology, The University of Alabama at Birmingham, United States of America

ARTICLE INFO

Keywords:
Preclinical research
In vivo small animal imaging
Pharmacokinetic studies
Positron emission
Molecular imaging
Performance evaluation

ABSTRACT

Preclinical nuclear molecular imaging speeds up the mean time from synthesis to market, in drug development process. Commercial imaging systems have in general high cost, require high-cost service contracts, special facilities and trained staff. In the current work, we present β-eye, a benchtop system for in vivo molecular screening of labeled compounds with Positron Emission Tomography (PET) isotopes. The developed system is based on a dual-head geometry, offering simplicity and decreased cost. The goal of the design is to provide 2D, real-time radionuclide images of mice, allowing the recording of fast frames and thus perform fast kinetic studies, with spatial resolution of $\sim$ 2 mm. Performance evaluation demonstrates the ability of β-eye to provide quantitative results for injected activities lower than 1.5 MBq, which is adequate for pharmacodynamic studies in small mice.

1. Introduction

Preclinical molecular imaging is increasingly being used as a valuable tool in the development of new imaging agents, as well as in drug development process (Cherry, 2004; Waaijer et al., 2018). Small animal imaging may help reduce attrition rates and mean time from synthesis to market in drug development process (Willmann et al., 2008). Moreover, it provides a robust alternative to ex-vivo biodistribution studies, a standard part of preclinical research, which introduce restrictions in the design of the experimental protocols and raises economical and ethical issues, due to the large number of required animals (Kagadis et al., 2016). Preclinical imaging solutions have a broad application field such as, cancer research; inflammation; neurology; cardiology; neuroimaging and infectious diseases.

Currently, among the numerous imaging techniques that fall under the umbrella of molecular imaging, Positron Emission Tomography (PET) is the most dominant one, as it typically provides the highest standards in terms of sensitivity, specificity and spatial resolution. In the preclinical field, PET has been standardized and nowadays it is widely used in a series of studies related with the nervous or cardiovascular system and oncology (James and Gambhir, 2012; Wu and Shu, 2018). This vital role of PET in the small animal imaging has been well recognized, and has attracted the interest both of the research community and industry. In particular, over the years, several research groups have developed prototype PET systems suitable for laboratory animals imaging, providing spatial resolution of 1.5–2 mm, and peak detection efficiency ranging from 1% to 5% (Lecomte et al., 1996; Cherry et al., 1996; Surti et al., 2003; McElroy et al., 2003; Raylman et al., 2006; Zhang et al., 2010a; Seidel et al., 2003; Vrigneaud et al., 2018; Amirrashedi et al., 2019). The majority of them rely on full-ring cylindrical geometries, while some groups have proposed partial rings or dual-head geometries, in order to reduce cost, at the expense of reduced count sensitivity and resolution. In addition to those, many preclinical PET scanners have been already introduced to the market.

As a reference, commercial PET scanners developed during the period 2000–2012, showed peak detection efficiency ranges between 1.2%–6.7% and spatial resolution between 1.6–3.2 mm in all three planes and different radial offsets (Goertzen et al., 2012). In the following years, technological advances in scintillation materials and photon detection, permitted the enhancement of scanners performance. The standards now in 3D PET imaging include spatial resolution between 0.7 and 1.3 mm, while sensitivity can reach values over 10% (Amirrashedi et al., 2020). Among others, Molecubes β-cube scanner provides spatial resolution $\sim$1 mm and absolute peak sensitivity of

* Corresponding author at: BIOEMTECH, Lefkippos Attica Technology Park - N.C.S.R Demokritos, Greece.
E-mail address: lfysikop@bioemtech.com (E. Fysikopoulos).

https://doi.org/10.1016/j.apradiso.2021.110034
Received 12 May 2021; Received in revised form 26 October 2021; Accepted 16 November 2021
Available online 1 December 2021

12.4%, using a full ring geometry based on monolithic LYSO — Silicon Photomultiplier (SiPM) detectors pairs (Krishnamoorthy et al., 2018); Sofie Biosciences G8 scanner provides spatial resolution ~0.9 mm and absolute peak sensitivity of 9% (Gu et al., 2018), using four opposing panel detectors based on pixelated BGO — Position Sensitive Photomultiplier Tube (PSPMT) detectors pairs; Bruker PET insert infers a spatial resolution of ~0.87 mm and peak sensitivity of 11% (Gsell et al., 2020). Mediso's nanoScan scanner provides spatial resolution ~0.9 mm and absolute peak sensitivity of 8.4% using a full ring geometry based on pixelated LYSO-PSPMT detectors pairs (Nagy et al., 2013). Lastly, the VECTor scanner by Milabs provides a spatial resolution near 0.9 mm and absolute peak sensitivity of 0.37% using 3 stationary flat-panel NaI(Tl) detectors and a clustered-pinhole collimator designed for simultaneous PET and SPECT tracers imaging (Walker et al., 2014).

While these performance characteristics of the latest 3D commercial scanners are valuable when it comes to resolve smaller features and improve quantification in optimized scan times, typically they are directly related with high purchase and maintenance costs. In addition, calibration and post-processing routines which are mandatory in high-end system configurations, do not permit any type of real-time imaging from zero-time to post-injection. In contrary, fast, real-time, 2D dynamic imaging prove to have several advantages for the whole preclinical routine, as it provides a time effective method to study new molecules and radiotracers with unknown accumulation behavior.

Taking into account the existing gap between ex vivo biodistribution studies and high performance 3D molecular imaging systems, we present the evaluation and performance characteristics of β-eye, a benchtop system, with footprint of 350 mm × 350 mm × 390 mm and weigh less than 30 kg, that allows real-time, 2D dynamic screening of labeled compounds with PET isotopes. β-eye is based on a dual-head geometry, offering simplicity and decreased cost, compared to typical cylindrical geometries. Main performance metrics to achieve were ~2 mm spatial resolution in the final 2D reconstructed image and ~1% system sensitivity at the center of the scanner adequate for typical pharmacokinetic studies (Palm et al., 2003; Zhang et al., 2010a). In this paper, we present the performance parameters following methodologies described previously for dual head geometries (Zhang et al., 2010a,b; Seidel et al., 2003). Phantom and in vivo animal studies have been performed to demonstrate the quantitative capabilities of this newly developed benchtop screening tool for preclinical imaging.

2. Materials and methods

2.1. β-eye system description

β-eye is a dedicated planar coincidence camera developed for live, real-time, fast screening of small animals injected with labeled compounds including peptides, antibodies and nanoparticles. Two detection heads are placed opposing each other at a spacing of 65 mm, in order to detect annihilation gammas from radiolabeled biomolecules (2D-PET). Each detector has a sensitive area of 48.3 mm × 96.6 mm, large enough to dynamic screen laboratory mices (18–40 g), which is a key feature to ensure real time imaging during scan, even at short frames. Fig. 1 represents a schematic drawing of the β-eye system. The external dimensions of the entire system, including the detectors, data acquisition electronics, high voltage modules, power supply and mechanical parts, are 350 mm × 350 mm × 390 mm, while its weight is less than 30 kg, achieving desirable portability. Connectors for delivering and evacuating gas anesthesia to and from the animal platform are externally provided in the back of the system. Anesthetization can be achieved upon the scanner allowing imaging at zero time post injection. A heating pad is located upon the imaging platform that actively maintains animal's body temperature at pre-set target value. Finally, a static optical image of the animal is provided, giving the outline of the mouse prior to acquisition. This image when fused with the corresponding nuclear one, provides a map of the mouse so as to understand in which organs the radioactivity is distributed. To further enhance anatomical mouse mapping to the corresponding functional information a deep neural network was used to translate the photographic mouse image to an artificially produced X-ray scan. A set of hundreds aligned input (photographic) /output (X-ray) images were acquired in order to train a well-established pix2pix network (Isola et al., 2016). The methodology followed is thoroughly described in Fysikopoulos et al. (2022). Results presented in the current study show that a X-ray image with sufficient accuracy for mouse anatomical mapping, but not for diagnosis, is predicted from the optical one.

β-Eye detectors. Each detector consists of a 21 × 42 pixelated bismuth germanate (BGO) scintillator array with a thickness of 6 mm (Hilger, UK). The individual crystal elements in the array have a cross-section size of 2 mm × 2 mm and a pitch size of 2.3 mm. The BGO array is coupled to two H12700 A multichannel PSPMTs (Hamamatsu Photonics, Japan) for scintillation light detection, covering a 48.3 mm × 96.6 mm field of view (FOV). A borosilicate glass window, 2.5 mm thick, covered with optical grease (BC-631, Saint Gobain) is used for coupling. A symmetric charge division resistor network is used to convert the anode outputs from the two PSPMTs into four position encoding signals (Popov, 2004). Four custom preamplifiers shape the position signals, taking into account the analog to digital converter (ADC) sampling rate.

Data acquisition electronics. The four positions signals of each detector are continuously sampled by 14 bits free running ADCs with 125 Msps sampling rate (FMC116, Abaco, US). The digitizer is connected, via a FMC connector, to an FPGA board (VC707, Xilinx, US), which contains also a 1 GB DDR3 SODIMM memory and a gigabit Ethernet, which are used in the current implementation for temporary data storage and transmission. A custom core was written in VHSIC Hardware Description Language (VHDL) describing the signal processing of the acquired digitized data. A digital version of the constant fraction discriminator (CFD) circuitry was implemented, in order to achieve a time resolution higher than the sampling period. List mode data are transmitted to a server running on a Linux machine, for postprocessing, using user datagram protocol (UDP) packets.

Image reconstruction. CASToR (Merlin et al., 2018), an open source multi-platform project for PET, SPECT and CT reconstruction is used to reconstruct 3D images from the limited angle projection data acquired on β-eye. The optimizer is the standard Maximum Likelihood Expectation Maximization (MLEM) algorithm. For a typical study, 10 iterations and a voxel size of 1.15 × 1.15 × 1.57 mm^3 are used for data reconstruction. Iterative optimization algorithms require the computation of a sensitivity image, requiring a backward projection step over all possible detection elements. This sensitivity image has been produced from an acquisition of a uniform object with high statistics generated by a Monte Carlo-based GATE simulation study. A 50 mm × 100 mm × 65 mm plastic phantom (Poly(methyl methacrylate) (PMMA)) filled with ^{18}F has been placed between the two modeled detectors of the simulated β-eye system and GATE results provided the required high statistics, in order to compute the sensitivity image. This method relies on the assumption that the data collected cover all possible lines of response, and is affected by the same geometry and normalization limitations.

In order to compensate for non-uniformities caused by variation in detector efficiency due to light collection and PSPMT non-uniformities a real experiment was conducted. A uniform (50 mm × 100 mm × 25 mm), 1.3 MBq flood source filled with 2-deoxy-2-[18F]fluoro-D-glucose ($[^{18}F]$FDG) has been placed in the midplane between the detectors and was imaged for 15 h, in order to generate a normalization factor for each line of response (LOR). Correction is afterwards performed by multiplying the measured LOR event with the corresponding normalization factor for that LOR. The final 2D-image is produced by summing the slices that corresponds to the area that the small animal is placed in the transverse plane (~25 mm around the midplane).

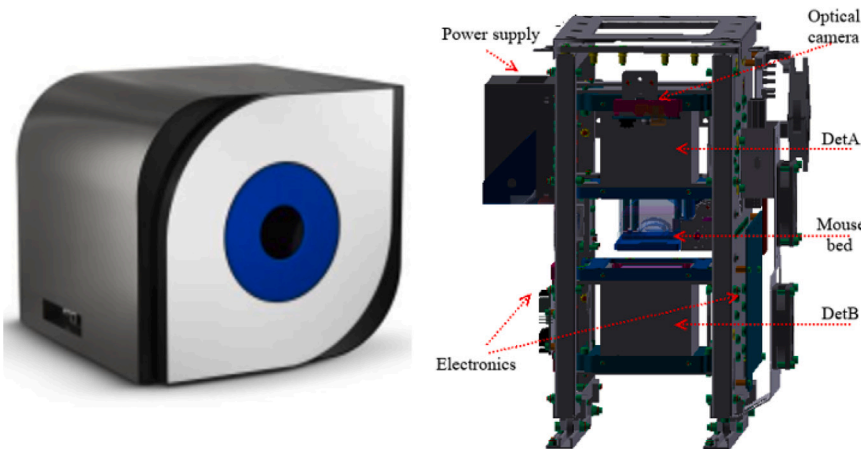

Fig. 1. Photograph of the β-eye system (left) and simplified 3D mechanical drawing (right).

Graphical user interface. β-eye comes with a pre-installed software that supports the conduction of static and/or dynamic studies with selectable time frames. The software is designed to concurrently display real time images with a refresh rate of 1 s, as well as a cumulative image that depicts the sum of all acquired frames up to that moment. In the former, coincidence data are grouped to projections in the central plane, using the non-iterative Focal Plane Tomography (FPT) algorithm (Efthimiou et al., 2013) and imaged every second providing real-time biodistribution measurements of the radiolabeled compound. In the latter, the 2D-image produced from the sum of CASToR reconstructed slices is imaged at the end of each frame. The lowest frame time that one may select is 10 s, due to the iterative nature of the reconstruction algorithm (MLEM). The software also provides all necessary tools for image viewing and processing. Kinetic curves can be automatically extracted from each frame of the dynamic studies and for various Regions-Of-Interests (ROIs) while all results can be stored in DICOM format for further processing.

2.2. Description of phantom studies

Performance characteristics of β-eye were determined experimentally using ^{22}Na and [^{18}F]FDG sources, following previously described methodologies for dual head geometries (Zhang et al., 2010a,b; Seidel et al., 2003; González et al., 2016).

Position mapping and energy resolution. Position mapping was achieved by placing a uniform, 1.3 MBq flood source filled with [^{18}F]FDG in the midplane between the detectors. Coincidence data have been acquired for 15 h, in order to achieve high statistics. Using the obtained raw flood image, a grid that maps each crystal pixel is determined for each detector. Afterwards, a look-up-table (LUT) of each raw image is extracted and the energy spectrum of each single crystal element is derived. Each spectrum is normalized to the same photopeak position by multiplying each value of the spectrum with the ratio of the normalized photopeak to the current photopeak. Normalized energy spectrum was derived by the sum of all individual spectra of the crystal elements, after corrections were applied for each pixel of the array. A Gaussian function was fitted to the normalized energy spectrum and the energy resolution was measured as the full width at half-maximum (FWHM) of the Gaussian function divided by the energy (511 keV). An wide energy window equal to 350–700 keV was used in the final set up to increase system sensitivity.

Coincidence timing resolution. For coincidence timing measurements, the aforementioned ^{22}Na point source was positioned in the center field of view (CFOV) in the midplane between the detectors. The differences in the arrival time between pairs of coincidence events were histogrammed and fitted with a Gaussian function. The FWHM of the fitted plot provides a measure of the coincidence timing resolution between the two detectors heads. A wide timing window equal to 16 ns was used in the final set up to increase system sensitivity.

Spatial resolution and sensitivity. The image spatial resolution and sensitivity of the β-eye system was measured using a 0.2 MBq ^{22}Na point source with a nominal size of 1 mm, embedded in an acrylic plastic (Spectrum Techniques, US). The source was attached to a 3D-printed phantom and positioned in the midplane between the two detectors. Starting from the center of FOV, the source was stepped across the central coronal plane towards its edges in both x and y directions. The step size was 5 mm for both x and y directions. The source was then stepped in a same manner in an off-center coronal plane (raised 6 mm along z direction). Acquisition time was 120 s for each measurement. The acquired data were histogrammed with an energy window of 350–700 keV. For the spatial resolution computation, the FWHM of the point spread function at all different positions was calculated in the final 2D image using Gaussian fit. System sensitivity was calculated as the ratio between the recorded total coincidence counting rate in the energy and timing windows and the source activity.

Count rate performance. Counting-rate performance of β-eye was evaluated using a cylindrical plastic tube (10 mm diameter and 40 mm height) filled with [^{18}F]FDG solution. The tube was positioned in the CFOV of the midplane between the detectors and coincidence data have been acquired until the total initial activity of 5.6 MBq decayed below 3.5 kBq.

Quantification. For the evaluation of system sensitivity to activity variations, five cylindrical phantoms (12 mm in diameter, 8 mm active height) filled with different concentrations of [^{18}F]FDG solutions were placed in the midplane of the two detectors. Coincidence data have been acquired for 10 min, using a time frame of 2 min usually used in dynamic mice studies. A dose calibrator (DC) was used in order to measure the precision of phantoms activity ratio. The actual ratios are equal to 1, 0.68, 0.51, 0.35, 0.19. The aforementioned ratios were also measured on the final reconstructed 2D images and the results were compared, in order to determine and quantify variations.

Fillable mouse phantom. In order to further evaluate the ability of the system to quantify activity variations, a fillable mouse phantom (Fillable mouse/rat phantom, BIOEMTECH, Greece) was used. The design of the mouse phantom is based on the Digimouse, a model of a 28 g mouse extracted from anatomical and cryosection data (Dogdas et al., 2007). The external dimensions of the phantom is in close proximity to the publication by the NEMA standard NU 4-2008 for performance measurements of small animal tomographs. A sketch of the phantom design is presented in Fig. 2. The internal organs were filled with

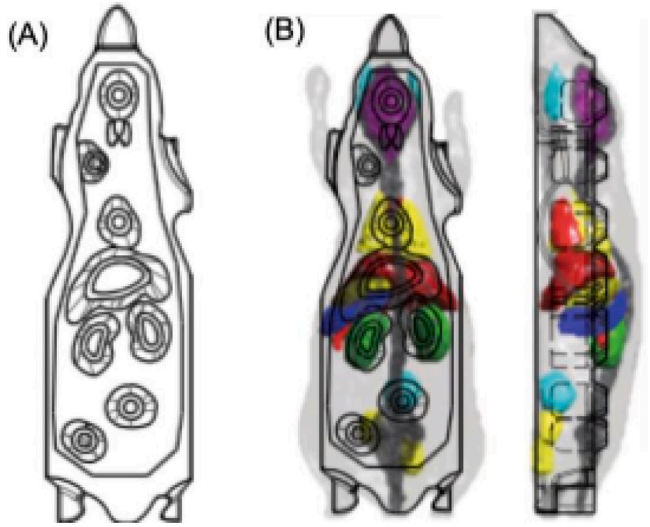

Fig. 2. (A) The mouse phantom design and all the internal organs. (B) Upper and side view of the mouse phantom, superimposed on the Digimouse 3D image.

[^{18}F]FDG solutions of measured activities and the phantom was imaged in β-eye for 20 min.

The values of percent injected dose per organ (%ID/organ) for the imaging experiments were calculated by quick scanning (5 min duration scan) the syringe before and after injection and then dividing the counts in each organ on the final reconstructed 2D image, by the calculated difference in counts of the syringe reconstructed image. This difference in syringe imaging corresponds to the injected dose in counts and all imaging data are decay-corrected to the same time point.

2.3. Description of animal studies

Several proof-of-concept studies were performed with different isotopes, to highlight both the dynamic imaging capability of the β-eye system and its efficient performance over a wide range of PET tracers.

In vivo studies with [^{18}F]FDG were performed on a healthy female Webster Swiss Albino mice of 3–5 weeks old. Scanning was performed for 1 h, following a tail vein injection of 655 kBq/160 uL [^{18}F]FDG. The acquisition time was set to 2 min for all acquired frames, leading to 30 frames in total. Lower frame duration down to 10 s/frame is feasible with β-eye, however not well suited in the aforementioned study.

In vivo studies with Co-55 were carried out on 5 weeks old female Nu/Nu mice implanted with different xenograft tumors. In vivo studies with Ga-68 were performed on 8–12 weeks old female C57BL/6 mice implanted with syngeneic murine colon carcinoma cells. [^{55}Co]-labeled SSTR2 targeting peptide was injected through the tail vein, having an activity of 1.332 MBq and scans were performed 4 h post-injection, for 20 min. [^{68}Ga]GZP was injected through the tail vein, with an activity of 3.33 MBq and imaged 1 h post-injection for 20 min.

Animals were anesthetized with isofluorane (3%–5% for induction and 1%–3% for maintenance) in all cases and kept warmed during all imaging scans. All animal procedures were approved by the General Directorate of Veterinary Services (Athens, Attica Prefecture, Greece) and by the Bioethical Committee of the Institution (Permit number: EL 25 BIO 022), on the basis of the European Directive 2010/63/EU on the protection of animals used for experimental purposes.

Quantification was performed on the β-eye embedded software and either %ID/organ was estimated, as described above, or ratios of tumour to kidney ratios were calculated, for scans where the syringe had not been scanned.

Table 1
β-eye detector performance characteristics.

Parameter	Measured value
Energy resolution (mean)	19.5%
Spatial resolution — Offset 0 mm (mean)	2.1 mm
Spatial resolution — Offset 6 mm (mean)	2.1 mm
Timing resolution	4 ns
System sensitivity at CFOV (350–700 keV)	0.9%

3. Results

3.1. Detector performance characteristics

The β-eye detector was fully characterized in terms of energy, spatial and timing resolution, system sensitivity and image uniformity. Fig. 3 shows the flood histogram of the top detector and the corresponding normalized energy spectrum, along with two profiles of the 16th column and 9th row. Most of the crystal elements in the 21 × 42 BGO array are clearly identified except pixels in the periphery, which do not affect the overall performance as that pixels are located at the edges of the field of view. The measured peak-to-valley ratios were measured equal to 1.7 (mean value) along the column direction and 1.4 (mean value) along the row direction. The energy resolution is 19.3% and 19.6% for top and bottom detector respectively. The energy resolution measured at the edges and in the middle of the detector was found equal to ~19–20% proving the uniform performance of the system.

The coincidence timing resolution of the detector pair was 4 ns FWHM. The FWTM has been found equal to 5 ns. Fig. 4 illustrates the distribution and the corresponding Gaussian fit. The achieved digital timing resolution is in good agreement with the 4.1 nsec achieved by other authors using a BGO-PSPMT detector pair and similar electronics (Zhang et al., 2010a).

The image spatial resolution was measured to range from 1.8 to 2.3 mm along coronal x and y axes in the midplane between the detectors (offset 0 mm – average equal to 2.1 mm) and when raised 6 mm along z direction (offset 6 mm – average equal to 2.1 mm). Fig. 5 shows the calculated spatial resolution values plotted against the distance from center for 0 mm and 6 mm offset in the z axis.

Fig. 6 (left) plots the measured system sensitivity as a function of the source location along both the coronal x and y directions. One can observe the degradation that occur as the source is moved from the CFOV to the edges in both x and y directions. The sensitivity image used in the CaSTOR reconstruction platform that has been produced from the acquisition of a uniform object with high statistics generated by the Monte Carlo-based GATE simulation study, corrects this non-uniformity in the final reconstructed image. Table 1 summarizes β-eye performance characteristics.

Fig. 6 (right) plots the coincidence count rate as a function of activity. β-eye prove to have a linear response for recorded counts plotted against activity and for activities lower than 1.5 MBq ($f(x) = 3.4 \cdot 10^5 \cdot x + 1.2 \cdot 10^4$, $R^2 = 0.98$), which is adequate for mice imaging studies with PET radioisotopes. The peak total counts rate is 545 kcpm (9 kcps) achieved at a total activity of 2.9 Mbq.

The reconstructed image of the five cylindrical phantoms used for the evaluation of system sensitivity dependency to activity variations is presented in Fig. 7. Ratios derived from dose calibrator measurements (actual values) along with ratios extracted from measured ROI values in the reconstructed images, are summarized in Table 2. We refer for simplicity, to the ratios measured in one time frame of 2 min duration, as they remain stable for all five acquired frames, during the 10 min acquisition. Results show the ability of β-eye system to quantify activity variations with high accuracy for 2 min time frames. As shown at the right of Fig. 7, good linearity is observed between the mean ROI image values and the activities.

Fig. 8 shows the reconstructed 2D image of the fillable mouse phantom which was used to further evaluate quantification capabilities

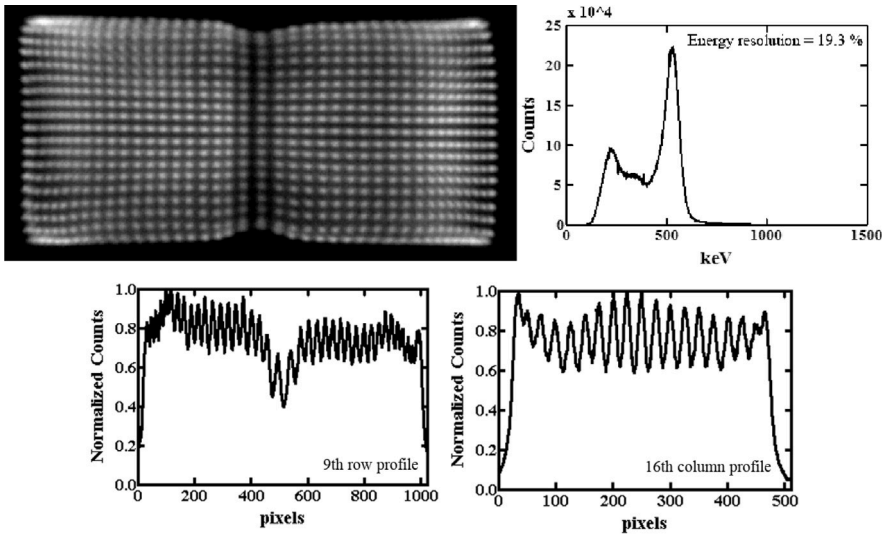

Fig. 3. Raw image and normalized energy spectrum of top detector.

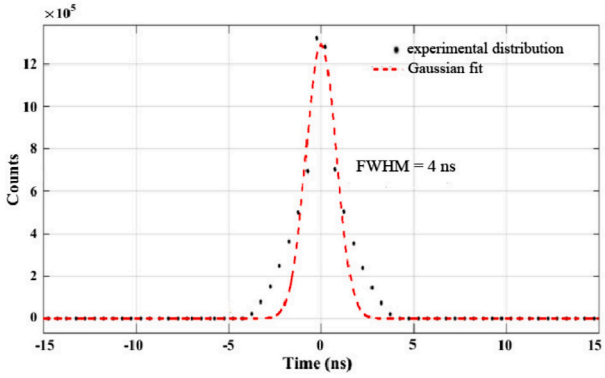

Fig. 4. Measured coincidence timing distribution. Experimental distribution (black) and corresponding Gaussian fit (red).

of β-eye system. The acquired [^{18}F]FDG image is illustrated on the left, while the nuclear image fussed with the optical one is presented on the right, proving that the optical photograph may be effectively used for organs mapping in the post processing of in vivo experiments. Measured values on dose calibrator (DC) along with measured ROI values in the reconstructed image are summarized in Table 3, as %ID/organ. Results show that accurate quantitative information is obtained even for more complicated structure such as the fillable mouse phantom.

3.2. In vivo mouse studies

Fig. 9 (top) shows ten selected reconstructed 2D images: (a) 0–2 min (Frame #1), (b) 2–4 min (Frame #2), (c) 4–6 min (Frame #3), (d) 6–8 min (Frame #4), (e) 8–10 min (Frame #5), (f) 20–22 min (Frame #10), (g) 30–32 min (Frame #15), (h) 40–42 min (Frame #20), (i) 50–52 min (Frame #25) and (k) 0–60 min (Summed), following the injection in the dynamic [^{18}F]FDG study. The reconstructed images show the activity accumulating in kidneys, bladder, heart and brain. The measured time-activity curve in the aforementioned organs was plotted and presented in Fig. 9 (bottom), in which one can clearly see the trend of activity distribution in these organs as time progresses.

Results of [^{55}Co]-labeled SSTR2 targeting peptide are shown in Fig. 10. Uptake can be clearly seen in the kidneys and in the subcutaneous tumor on the left shoulder. Tumor to liver ratio is calculated as 0.07, providing an immediate quantitative evaluation of the tumor targeting.

Lastly, results of [^{68}Ga]GZP are shown in Fig. 11. Uptake can be seen in the kidneys and tumor, as expected and also in the bladder as the tracer is cleared away from the body. A tumor to kidney ratio, of 0.7 is calculated right by the end of the scan, providing a quantitative evaluation of the tumor targeting.

Figs. 10 and 11 demonstrate also the fusion of the nuclear images with the corresponding optical (left) and the artificial X-ray (right). It is indisputable that the anatomical mouse mapping is greatly enhanced with the predicted X-ray, if compared with the optical one.

4. Discussion and conclusions

Performance evaluation of β-eye demonstrates its ability to be used as an efficient standard screening tool for radiolabeled compounds with PET isotopes. Although in this work, system is not evaluated according to NEMA protocol, through a series of experiments, we demonstrate that system fulfills all design goals that were set based on the preclinical research needs. β-eye is mostly a platform, whose main features are overall small size, ability to provide images during the scan and field of view that allows whole body mouse images. Thus, most of this work was focused on designing the entire system, mechanical and mouse support parts, as well as visualization software, which were integrated with two opposite detector heads. Although we selected PSPMTs coupled to BGO for the proof of concept system, the key detectors can be easily replaced with other more efficient combinations of scintillators and SiPMs.

The system spatial resolution was found to be on average 2.1 mm across the FOV, while sensitivity reaches the 0.9% at the CFOV. Energy and timing resolution were determined at ~19% and 4 ns respectively. In terms of the count rate, for doses up to 1.5 MBq, β-eye showed a linear response of the recorded counts as a function of the activity, while the maximum total rate was estimated at 9 kcps (at 2.9 MBq). In addition, through a series of phantom and in-vivo studies, we demonstrate that the system permits a quite accurate quantification of the activity variations across the FOV, as well as enables the possibility for real time imaging in very short time frames. β-eye can very efficiently be used for the extrapolation of quantitative results in different time points at the same animal and over a long period, leading to significant savings in time, cost and number of animals. Moreover, by enabling the non-invasive quantification and visualization of the accumulation of a tracer at the first minutes post injection, ex-vivo protocols can be rapidly evaluated and optimized.

All these characteristics, as vital as they are for pharmacokinetics and other studies, are all integrated in a compact and benchtop system

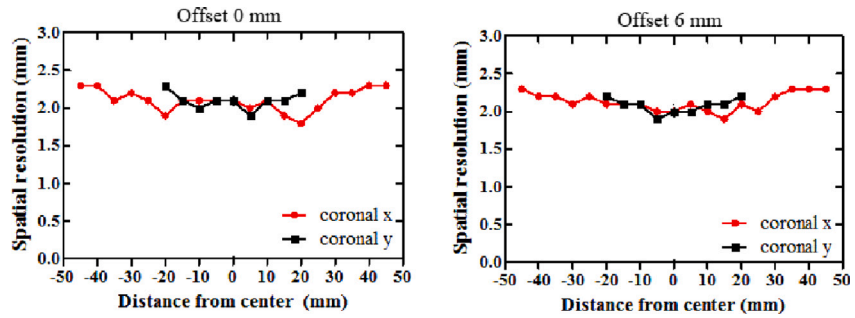

Fig. 5. Spatial resolution along coronal x and y in the midplane (left) and when raised 6 mm along z direction (right).

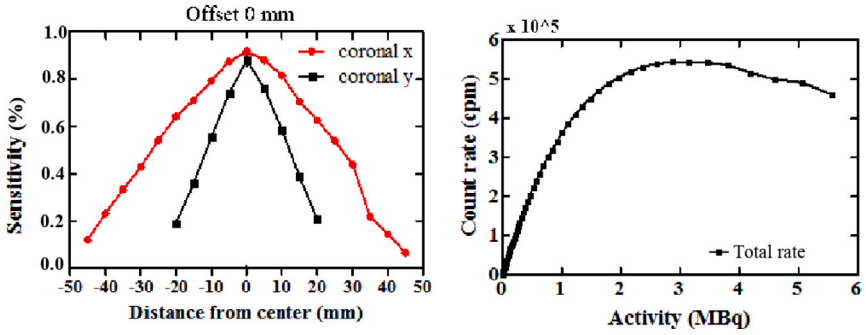

Fig. 6. Measured system sensitivity as function from the center in both coronal x and y directions (left), Measured count rate as a function of activity (right).

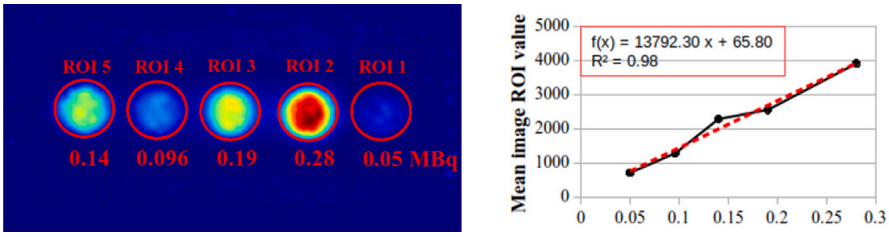

Fig. 7. Five cylindrical phantoms filled with [^{18}F]FDG solutions of actual activity ratio 0.19, 1, 0.68, 0.35, 0.51 (from right to left). The mean ROI values are plotted as a function of well calibrated activities and shown at the bottom of the figure.

Table 2
Actual and measured ratios of the cylindrical phantoms.

Corresponding ROI	Actual ratio	Measured ratio	Percent deviation (%)
ROI 1/ROI 2	0.19	0.18	5.3
ROI 2/ROI 2	1.00	1.00	0.0
ROI 3/ROI 2	0.68	0.65	4.4
ROI 4/ROI 2	0.35	0.33	5.7
ROI 5/ROI 2	0.51	0.58	13.7

Table 3
Actual and measured %ID/organ of the fillable mouse phantom.

Organ	%ID/organ from DC	%ID/organ from image	Percent deviation (%)
Lower tumor	7.1	6.7	5.6
Bladder	10.5	9.8	6.7
L. Kidney	12.7	12.3	3.1
R. Kidney	12.7	12.5	1.6
Liver	23.8	19.7	17.2
Heart	9.9	8.4	15.2
Upper tumor	4.8	4.6	4.2
Thyroid	12.0	13.8	15.0
Brain	6.6	6.9	4.5

which can serve as a great alternative over standard ex-vivo biodistribution techniques, or costly 3D scanners. In terms of performance, all design goals, set based on the preclinical research needs, were accomplished. As expected, in comparison with commercial 3D PET scanners, some of its performance characteristics are inferior. One of those, is the sensitivity which in β-eye does not exceed the 1%, while in modern state-of-the-art scanners can be over 12%. Although part of the reason for this difference is related to the type of electronics and scintillators, the key reason lies on the dual head-based geometry and the lack of full angular coverage of the object of study. In addition to that, β-eye shows lower count rate capabilities with respect to other systems. Lastly, spatial resolution is slightly worst compared to the modern standards, as 3D scanners that can reach submillimeter resolution have been already presented.

Although β-eye performance is not in the range of modern state-of-the-art 3D scanners, through this work we demonstrate that the overall scope of the design is not affected. The system creates an efficient imaging solution, widely accessible for a series of applications, which stands between ex vivo biodistribution and advanced 3D imaging. 2D real time screening of PET radiotracers and longitudinal studies in mice bearing tumors can be conducted with injected activities between 1 and 1.5 MBq very effectively.

Overall, the performance, size and simplicity in use make β-eye an efficient tool for groups already working with radioactivity, with no or limited access to large imaging systems, for the fast screening and initial

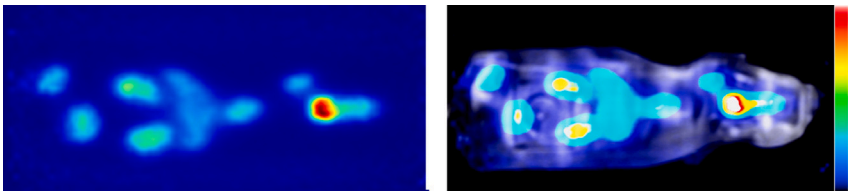

Fig. 8. Fillable mouse sized phantom. [^{18}F]FDG image of internal organs (left), [^{18}F]FDG image fussed with the optical one provided in β-eye system for ROI mapping (right). The color bar indicates the difference in accumulated activity (purple being the lowest and white the highest level of accumulation). (For interpretation of the references to color in this figure legend, the reader is referred to the web version of this article.)

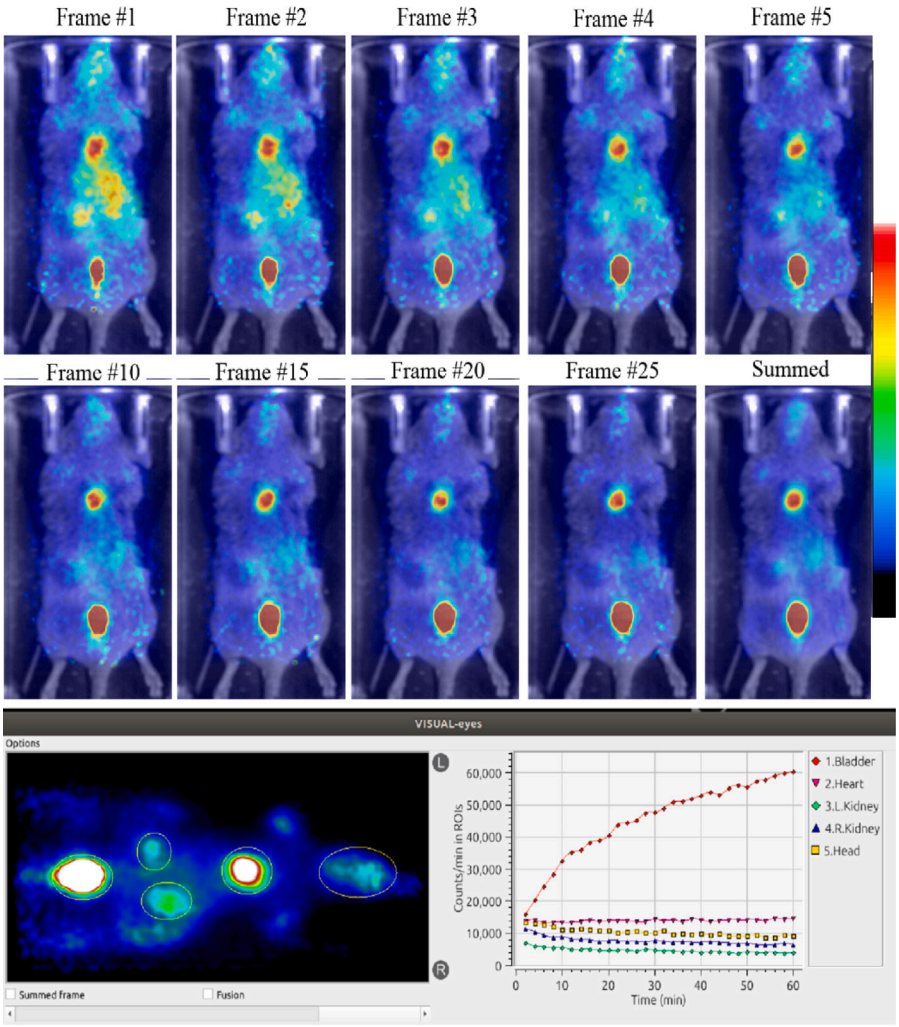

Fig. 9. Top: Selected frames from 1 h dynamic scan of a healthy mouse following a tail injection of 655 kBq/160 uL [^{18}F]FDG. The color bar indicates the difference in accumulated activity (purple being the lowest and white the highest level of accumulation); Bottom: Time activity curve in major organs of a healthy mouse during a 1 h dynamic [^{18}F]FDG scan. (For interpretation of the references to color in this figure legend, the reader is referred to the web version of this article.)

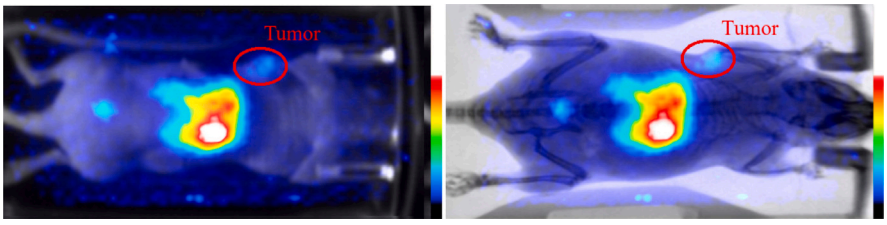

Fig. 10. 2D reconstructed image showing the uptake of [^{55}Co]-labeled SSTR2 targeting peptide, in the kidneys and in the subcutaneous tumor on the left shoulder. Fusion of the nuclear image with the optical (left) and the artificial X-ray (right). The color bar indicates the difference in accumulated activity (purple being the lowest and white the highest level of accumulation). (For interpretation of the references to color in this figure legend, the reader is referred to the web version of this article.)

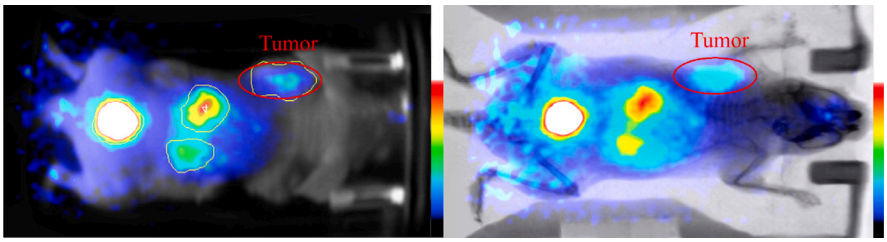

Fig. 11. 2D reconstructed image showing the uptake of [^{68}Ga]GZP in the kidneys and tumor, as expected and also in the bladder as the tracer is cleared away from the body. Fusion of the nuclear image with the optical (left) and the artificial X-ray (right). The color bar indicates the difference in accumulated activity (purple being the lowest and white the highest level of accumulation). (For interpretation of the references to color in this figure legend, the reader is referred to the web version of this article.)

evaluation of radiolabeled compounds. β-eye can be used: (a) as a standalone fast screening imaging tool including but not limited to oncology applications, providing static and dynamic imaging of mice from time-zero injection time; and/or (b) as a quality control tool complementing biodistribution and 3D imaging studies. Taking into account that a large portion of the published work on new probes uses radiolabelling but only biodistribution studies (or indicative images in clinical systems), one can argue that several research groups and the community as a whole would benefit from such an imaging system. β-eye may provide answers to the following basic questions: Do biomolecules reach the specific target that they are designed for? How long do they stay there? How long do they remain in the blood circulation? Are they stable over time? Do they concentrate in other organ/tissues? Thus, it can serve as a daily use preclinical imager, answering critical questions during the early stage of the development of a new probe, where small variations in synthetic procedures can affect its in vivo behavior.

Nevertheless, a technical upgrade of β-eye is undergoing. Based on previous studies, the transition to SiPMs, faster electronics and lutetium based scintillators can be translated to a cutting-edge performance (Lamprou et al., 2020a,b). Among other specifications, it is expected that the next generation of β-eye will infer better sensitivity, higher count rate capabilities, improved spatial and energy resolution and lastly, Time-Of-Flight capabilities. The simplicity of the concept eventually can be implemented in an inexpensive way – even using state of art detectors – placing such a system in the category of lab equipment and providing an additional tool to improve early testing of PET radiotracers.

Declaration of competing interest

One or more of the authors of this paper have disclosed potential or pertinent conflicts of interest, which may include receipt of payment, either direct or indirect, institutional support, or association with an entity in the biomedical field which may be perceived to have potential conflict of interest with this work. For full disclosure statements refer to https://doi.org/10.1016/j.apradiso.2021.110034. Eleftherios Fysikopoulos and Nikolaos Cheimarios report grants from Co financed by the European Regional Development Fund of the European Union and Greek national funds through the Operational Program Competitiveness, Entrepreneurship and Innovation, under the call RESEARCH - CREATE -INNOVATE, project code: T1EΔK-01159 with acronym NAVIGATE, during the conduct of the study.

Eleftherios Fysikopoulos, Dimitrios Glotsos, Spiros Kostopoulos and Maritina Rouchota report grants from Co-financed by Greece and the European Union (European Social Fund-ESF) through the Operational Program "Human Resources Development, Education and Lifelong Learning 2014-2020" in the context of the project "Deep learning algorithms for molecular imaging applications" (MIS-5050329), during the conduct of the study.

Suzzane Lapi reports grants from Navidea, grants from Cytosite, grants from ImaginAb, grants from Clovis, grants from Sanofi, outside the submitted work.

Anna Sorace reports grants from NIH NCI during the conduct of the study.

Efthymios Lamprou and Sophia Sarpaki are currently coworkers of BIOEMTECH, Nikolaos Cheimarios and Christos Sfyris were coworkers of BIOEMTECH during 2019/20. Eleftherios Fysikopoulos, Maria Georgiou, Maritina Rouchota and George Loudos own stock in BIOEMTECH.

Acknowledgments

This research has been co-financed by the European Regional Development Fund of the European Union and Greek national funds through the Operational Program Competitiveness, Entrepreneurship and Innovation, under the call RESEARCH - CREATE - INNOVATE, project code: T1EΔK-01159 with acronym NAVIGATE.

This research has also been co-financed by Greece and the European Union (European Social Fund-ESF) through the Operational Program "Human Resources Development, Education and Lifelong Learning 2014-2020" in the context of the project "Deep learning algorithms for molecular imaging applications" (MIS-5050329).

We thank the UAB Comprehensive Cancer Center's Preclinical Imaging Shared Facility P30CA013148 and partial support from American Cancer Society RSG-18-006-01-CCE and National Cancer Institute, United States R01CA240589.

References

Amirrashedi, M., Sarkar, S., Ghafarian, P., Shahraki, R.H., Geramifar, P., Zaidi, H., Ay, M., 2019. Nema NU-4 2008 performance evaluation of xtrim-PET: A prototype sipm-based preclinical scanner. Med. Phys. 46 (11), 4816–4825. http://dx.doi.org/10.1002/mp.13785.

Amirrashedi, M., Zaidi, H., Ay, M., 2020. Towards quantitative small-animal imaging on hybrid pet-ct and pet-mri systems. Clin. Transl. Imaging 8, 243–263. http://dx.doi.org/10.1007/s40336-020-00376-y.

Cherry, S.R., 2004. In vivo molecular and genomic imaging: New challenges for imaging physics. Phys. Med. Biol. 3 (7), http://dx.doi.org/10.1088/0031-9155/49/3/r01.

Cherry, S., Shao, Y., Siegel, S., Silverman, R., Meadors, K., Young, J., Jones, W., Newport, D., Moyers, C., Mumcuoglu, E., Chatziioannou, A., Farquhar, T., Andreaco, M., Paulus, M., Binkley, D., 1996. Micropet: A high resolution pet scanner for imaging small animals. In: IEEE Nucl Sci Symp Med Imag Conf, Vol. 2. pp. 1120–1124.

Dogdas, B., Stout, D., Chatziioannou, A.F., Lathy, R.M., 2007. Digimouse: a 3d whole body mouse atlas from ct and cryosection data. Phys. Med. Biol. 52 (3), http://dx.doi.org/10.1088/0031-9155/52/3/003.

Efthimiou, N., Loudos, G., Karakatsanis, N.A., Panayiotakis, G.S., 2013. Effect of intrinsic radioactivity on dual head pet system imaging and data acquisition simulation and experimental measurements. Med. Phys. 40 (11), http://dx.doi.org/10.1118/1.4824694.

Fysikopoulos, E., Rouchota, M., Eleftheriadis, V., Gatsiou, C.-A., Pilatis, I., Sarpaki, S., Loudos, G., Kostopoulos, S., Glotsos, D., 2022. Photograph to X-ray image translation for anatomical mouse mapping in preclinical nuclear molecular imaging. In: Proceedings of 2021 International Conference on Medical Imaging and Computer-Aided Diagnosis (MICAD 2021). Springer Singapore, pp. 302–311. http://dx.doi.org/10.1007/978-981-16-3880-0_31.

Goertzen, A.L., Bao, Q., Bergeron, M., Blankemeyer, E., Blinder, S., Cañadas, M., Chatziioannou, A.F., Dinelle, K., Elhami, E., Jans, H.-S., Lage, E., Lecomte, R., Sossi, V., Surti, S., Tai, Y.-C., Vaquero, J.J., Vicente, E., Williams, D.A., Laforest, R., 2012. Nema NU 4-2008 comparison of preclinical PET imaging systems. J. Nucl. Med. 53 (8), 1300—1309. http://dx.doi.org/10.2967/jnumed.111.099382.

González, A.J., Aguilar, A., Conde, P., Hernández, L., Moliner, L., Vidal, L.F., Sánchez, F., Sánchez, S., Correcher, C., Molinos, C., Barberá, J., Lankes, K., Junge, S., Bruckbauer, T., Bruyndonckx, P., Benlloch, J.M., 2016. A pet design based on sipm and monolithic lyso crystals: Performance evaluation. IEEE Trans. Nucl. Sci. 63 (5), 2471–2477. http://dx.doi.org/10.1109/TNS.2016.2522179.

Gsell, W., Molinos, C., Correcher, C., Belderbos, S., Wouters, J., Junge, S., Heidenreich, M., Velde, G., Rezaei, A., Nuyts, J., Cawthorne, C., Cleeren, F., Nannan, L., Deroose, C., Himmelreich, U., Gonzalez, A., 2020. Characterization of a preclinical pet insert in a 7 tesla mri scanner: beyond nema testing. Phys. Med. Biol. 65 (24), http://dx.doi.org/10.1088/1361-6560/aba08c.

Gu, Z., Taschereau, R., Vu, N., Prout, D.L., Silverman, R.W., Lee, J., Chatziioannou, A.F., 2018. Performance evaluation of g8, a high sensitivity benchtop preclinical pet/ct tomograph. J. Nucl. Med. http://dx.doi.org/10.2967/jnumed.118.208827.

Isola, P., Zhu, J., Zhou, T., Efros, A.A., 2016. Image-to-image translation with conditional adversarial networks. CoRR abs/1611.07004 arXiv:1611.07004 URL: http://arxiv.org/abs/1611.07004.

James, M., Gambhir, S., 2012. A molecular imaging primer: modalities imaging agents and applications. Physiol. Rev. 92, http://dx.doi.org/10.1152/physrev.00049.2010.

Kagadis, G., Ford, N., Karnabatidis, D., Loudos, G., 2016. Hanbook of Small Animal Imaging. CRC Press.

Krishnamoorthy, S., Blankemeyer, E., Mollet, P., Surti, S., Holen, R.V., Karp, J.S., 2018. Performance evaluation of the molecubes β -cube-a high spatial resolution and high sensitivity small animal pet scanner utilizing monolithic lyso scintillation detectors. Phys. Med. Biol. 27 (63), http://dx.doi.org/10.1088/1361-6560/aacec3.

Lamprou, E., Gonzalez, A.J., Sanchez, F., Benlloch, J.M., 2020a. Exploring tof capabilities of pet detector blocks based on large monolithic crystals and analog sipms. Phys. Med. 70, 10–18. http://dx.doi.org/10.1016/j.ejmp.2019.12.004.

Lamprou, E., Sanchez, F., Benlloch, J.M., Gonzalez, A.J., 2020b. In-depth evaluation of tof-pet detectors based on crystal arrays and the tofpet2 asic. Nucl. Instrum. Methods Phys. Res. A 977, 164295. http://dx.doi.org/10.1016/j.nima.2020.164295.

Lecomte, R., Cadorette, J., Rodrigue, S., Lapointe, D., Rouleau, D., Bentourkia, M., Yao, R., Msaki, P., 1996. Initial results from the sherbrooke avalanche photodiode positron tomograph. IEEE Trans. Nucl. Sci. 43 (3), 1952–1957. http://dx.doi.org/10.1109/23.507252.

McElroy, D., Pimpl, W., Djelassi, M., Pichler, B., Rafecas, M., Schuler, T., Ziegler, S., 2003. First results from madpet-ii: a novel detector and readout system for high resolution small animal pet. In: 2003 IEEE Nuclear Science Symposium. Conference Record (IEEE Cat. No.03CH37515), Vol. 3. pp. 2043–2047. http://dx.doi.org/10.1109/NSSMIC.2003.1352282.

Merlin, T., Stute, S., Benoit, D., Bert, J., Carlier, T., Comtat, C., Filipovic, M., Lamare, F., Visvikis, D., 2018. Castor: a generic data organization and processing code framework for multi-modal and multi-dimensional tomographic reconstruction. Phys. Med. Biol. 63 (18), http://dx.doi.org/10.1088/1361-6560/aadac1.

Nagy, K., Tóth, M., Major, P., Patay, G., Egri, G., Häggkvist, J., Varrone, A., Farde, L., Halldin, C., Gulyás, B., 2013. Performance evaluation of the small-animal nanoscan pet/mri system. J. Nucl. Med. 54 (10), 1825–1832. http://dx.doi.org/10.2967/jnumed.112.119065.

Palm, S., Enmon, R.M., Matei, C., Kolbert, K.S., Xu, S., Zanzonico, P.B., Finn, R.L., Koutcher, J.A., Larson, S.M., Sgouros, G., 2003. Pharmacokinetics and biodistribution of 86y-trastuzumab for 90y dosimetry in an ovarian carcinoma model: Correlative micropet and MRI. J. Nucl. Med. 44 (7), 1148–1155.

Popov, V., 2004. Matrix output device readout system. US6747263B1.

Raylman, R.R., Majewski, S., Lemieux, S.K., Velan, S.S., Kross, B., Popov, V., Smith, M.F., Weisenberger, A.G., Zorn, C., Marano, G.D., 2006. Simultaneous MRI and PET imaging of a rat brain. Phys. Med. Biol. 51 (24), 6371–6379. http://dx.doi.org/10.1088/0031-9155/51/24/006.

Seidel, J., Xi, W., Kakareka, J.W., Pohida, T.J., Jagoda, E., Green, M.V., Choyke, P.L., 2003. Performance characteristics of a positron projection imager for mouse whole-body imaging. Nucl. Med. Biol. 40 (3), 321–330. http://dx.doi.org/10.1016/j.nucmedbio.2012.12.003.

Surti, S., Karp, J., Perkins, A., Freifelder, R., Muehllehner, G., 2003. Design evaluation of a-pet: A high sensitivity animal PET camera. IEEE Trans. Nucl. Sci. 50 (5), 1357–1363. http://dx.doi.org/10.1109/TNS.2003.817950.

Vrigneaud, J., McGrath, J., Courteau, A., Pegg, R., Gomis, A., Camacho, A., Martin, G., Schramm, N., Brunotte, F., 2018. Initial performance evaluation of a preclinical PET scanner available as a clip-on assembly in a sequential PET-mri system. Phys. Med. Biol. 63 (12), http://dx.doi.org/10.1088/1361-6560/aac4f7.

Waaijer, S.J., Kok, I.C., Eisses, B., Schröder, C.P., Jalving, M., Brouwers, A.H., Lub-de Hooge, M.N., de Vries, E.G., 2018. Molecular imaging in cancer drug development. J. Nucl. Med. 59 (5), 726–732. http://dx.doi.org/10.2967/jnumed.116.188045.

Walker, M.D., Goorden, M.C., Dinelle, K., Ramakers, R.M., Blinder, S., Shirmohammad, M., van der Have, F., Beekman, F.J., Sossi, V., 2014. Performance assessment of a preclinical PET scanner with pinhole collimation by comparison to a coincidence-based small-animal PET scanner. J. Nucl. Med. 55 (8), 1368–1374. http://dx.doi.org/10.2967/jnumed.113.136663.

Willmann, J.K., van Bruggen, N., Dinkelborg, L.M., Gambhir, S.S., 2008. Molecular imaging in drug development. Nat. Rev. Drug Discov. 7, http://dx.doi.org/10.1038/nrd2290.

Wu, M., Shu, J., 2018. Multimodal molecular imaging: Current status and future directions. Contrast Media Mol. Imaging 5, http://dx.doi.org/10.1155/2018/1382183.

Zhang, H., Bao, Q., Vu, N.T., Silverman, R.W., Taschereau, R., Berry-Pusey, B.N., Douraghy, A., Rannou, F.R., Stout, D.B., Chatziioannou, A.F., 2010a. Performance evaluation of petbox: A low cost bench top preclinical pet scanner. Mol. Imag. Biol. 13 (5), 949–961. http://dx.doi.org/10.1007/s11307-010-0413-y.

Zhang, H., Vu, N.T., Bao, Q., Silverman, R.W., Berry-Pusey, B.N., Douraghy, A., Williams, D.A., Rannou, F.R., Stout, D.B., Chatziioannou, A.F., 2010b. Performance characteristics of BGO detectors for a low cost preclinical PET scanner. IEEE Trans. Nucl. Sci. 57 (3), http://dx.doi.org/10.1109/tns.2010.2046753.